Journal of Materials Chemistry

Dynamic Article Links

Cite this: *J. Mater. Chem.*, 2012, **22**, 22575

www.rsc.org/materials

PAPER

Dextran based pH-sensitive near-infrared nanoprobe for *in vivo* differential-absorption dual-wavelength photoacoustic imaging of tumors†

Guojia Huang,[a] Zhan Si,[b] Sihua Yang,[a] Cong Li*[b] and Da Xing*[a]

Received 20th June 2012, Accepted 7th September 2012
DOI: 10.1039/c2jm33990k

A dextran based pH-sensitive near-infrared nanoprobe was prepared and applied as a contrast agent for photoacoustic imaging to identify a tumor *in vivo*. The nanoprobe has two resonance absorption peaks in the near-infrared region and the cleavage of hydrazone bonds in the low pH value environment can cause their coefficients to change, making a different ratio of photoacoustic signal output. By comparing the photoacoustic signal ratio under the two wavelengths, *in vitro* photoacoustic images show that the nanoprobe has the capacity to distinguish cancer cells and normal cells. Moreover, an *in vivo* mouse breast tumor model (EMT-6 cells) can be identified from peripheral normal tissues by dual-wavelength photoacoustic imaging. These results suggest the potential application of this pH-sensitive near-infrared nanoprobe as a contrast agent to noninvasively detect tumors in their early stage with high optical contrast by dual-wavelength photoacoustic imaging based on the tunable absorbance ratio in normal physiological and tumor acidic microenvironments.

1. Introduction

Diagnosis of tumors in their early stages is crucial to improve cancer patient survival and treatment outcomes. Currently, several methods are employed for cancer diagnosis, including X-ray, ultrasonography and nuclear magnetic resonance imaging (MRI).[1] X-ray is widely used in cancer detection, but it is a radiating imaging method and its sensitivity is limited in weak soft tissue. Ultrasonography is a safe method for cancer detection, but suffers from its high false-positive rate. MRI can supply a volume of information about a tumor, but it loses information about the edge. They differ from one another in terms of detection sensitivity, spatial temporal resolution, signal-to-noise ratio and quantitative accuracy.[2,3] Hence, it is often desirable to employ a imaging modality combining nanomaterials based angiography with high sensitivity, resolution and contrast to diagnosis and monitor the tumor and therapy.

Photoacoustic (PA) imaging, an emerging, noninvasive, nonionizing, deeply penetrating biomedical imaging modality, which can overcome the limitations of purely optical imaging methods that result from the intense optical scattering in soft tissue and combine the spectroscopic capability of light with the spatial resolution of ultrasound, may lead to a new medical imaging technique.[4,5] In PA imaging, a nonionizing short-pulsed laser is used as an excitation source to generate an acoustic signal resulting from thermoelastic expansion of the absorbent, which is then detected and used to recover the geometry of the object. Compared to other optical technologies, such as fluorescence imaging, PA imaging has a 100% relative sensitivity to optical absorption and can provide an image in a region up to several centimeters deep in biological tissue.[6] As optical absorption is strongly associated with various physiological parameters (most notably, the hemoglobin oxygen saturation), different tissues with various optical absorption coefficients produce distinguishable PA signals.[7] PA imaging has drawn great interest from various biomedical research fields and has been used to image tumors, blood vessels, hemoglobin oxygenation, and single cells in the absence and presence of contrast agents.[8–11] PA imaging provides femtomolar sensitivity and high temporal and spatial resolution.[12,13]

One of the important promises of nanotechnology is the development of techniques and tools for cancer diagnosis and therapy using safe, noninvasive, low-cost means.[14,15] Magnetite nanoparticles have recently attracted a great deal of attention by virtue of their potential biomedical applications, including MRI contrast enhancement and microwave-induced thermoacoustic tomography.[16,17] Upconversion nanoparticles are widely used for fluorescence bioimaging.[18,19] Carbon nanotubes also show an effective application in detection, imaging and drug delivery of cancer cells and tumor tissues.[20,21] Most current PA contrast

[a]*MOE Key Laboratory of Laser Life Science & Institute of Laser Life Science, College of Biophotonics, South China Normal University, Guangzhou 510631, China. E-mail: xingda@scnu.edu.cn; Fax: +86-20-85216052; Tel: +86-20-85210089*

[b]*Key Laboratory of Smart Drug Delivery, Ministry of Education & PLA, School of Pharmacy, Fudan University, Shanghai 201203, China. E-mail: congli@fudan.edu.cn; Fax: +86 21 5198 0100; Tel: +86 21 5198 0100*

† Electronic supplementary information (ESI) available: The detailed synthesis procedure of **NP1**, spectra, PA system, cell viabilities, absorbance of IR-783 and rhodamine, intracellular destination of **NP1** and histological examination. See DOI: 10.1039/c2jm33990k

agents, such as gold nanoparticles and a metabolite dye for cell or tumor imaging, employ high absorption coefficients at a certain wavelength.[22,23] They accumulate in the desired area of interest by targeting the tumor-associated receptor over-expressed on the cancer cell membrane[24,25] or through the enhanced permeability and retention (EPR) effect.[26,27] Gold nanoparticles exhibit a size and morphology dependent surface plasmon resonance absorbance band that is centered at 520 nm for 5 nm particles and shifts into the near-infrared (NIR) region for larger spherical clusters or nonspherical morphologies, such as nanorods.[28,29] But a problem with the application of these larger colloids *in vivo* is ultimate clearance or toxicity associated with mechanical blockage.[30] Furthermore, the performance of these probes *in vivo* is usually less satisfactory than that in cell cultures due to the unpredictable expression level of the tumor-associated receptors that closely depends on the tumor types and developmental stages. Compared with the tumor-associated receptors, tumor microenvironment indicators, including acidosis[31] and hypoxia,[32] are a universal phenomena of solid tumors, regardless of the tumor types or their developmental stages. The acidic extracellular environment induced by glycolysis under hypoxic conditions is perhaps the most pervasive in tumor microenvironments. Compared with the limited concentration of tumor-associated receptors, the bulky properties of the acidic tumor interstitium are much easier to access.[33] Therefore, PA probes sensing tumor microenvironments are promising for detecting tumors in their early stage with high optical contrast *in vivo*.

Here, we report a novel dextran based pH-sensitive near-infrared (NIR) nanoprobe (**NP1**) with the potential for dual-wavelength PA imaging to detect tumors *in vivo* by sensing tumor acidic microenvironments. The pH-sensitive **NP1**, as a PA probe, possesses many advantages. Firstly, dextran derivatives are degradable *in vivo* and are widely used in the clinic.[34] Secondly, nano-scaled dextrans can accumulate passively into tumor interstitium due to the EPR effect,[35] expected to further increase their tumor specificity. Finally, **NP1** demonstrated two pH-tunable resonance absorption peaks in the NIR region, in which the biological tissue shows the minimized absorption and PA has higher penetration depths.[36]

2. Methods and materials

2.1 Materials

All organic solvents were analytical grade from Fisher Scientific (Pittsburgh, PA, USA) unless otherwise specified. Dextran–NH_2 (20 kDa) was purchased from Duly biology (Nanjing, China), PEG^{2k}–NHS was purchased from JenKem Technology Co. Ltd (Beijing, China). Chloroacetic acid, 1,2-ethylenediamine, sodium periodate and hydrazine anhydrous were purchased from Sigma-Aldrich (St. Louis, MO, USA). Rhodamine succinimidyl ester, fetal bovine serum, penicillin, streptomycin and cell culture media were from Invitrogen (Carlsbad, CA, USA). MTT cell proliferation kit, Murine mammary tumor line EMT-6 cells and Swiss mouse embryo line 3T3 cells were obtained from American Type Culture Collection (Rockville, MD, USA). Water was purified using a Millipore Milli-Q Synthesis water system (Billerica, MA).

2.2 Synthesis of NP1

To a solution of IR-783 in 2 ml anhydrous DMF, 3-mercaptopropionic acid and triethylamine were added. The green color solution was allowed to stir in the dark at room temperature for 15 h and produced compound **1**. Then, *tert*-butyl carbazate was added under EDC and HOB as condensation agents to obtain compound **2**. To obtain compound **3**, compound **2** was dissolved in a mixture of DCM and TFA and stirred at room temperature for 1 h. The solvent was removed under a vacuum and the residue was redissolved in distilled water. Meanwhile, dextran reacted with chloroacetic acid sodium salt to give conjugate **4**, which was further reacted with ethylenediamine to obtain compound **5**. The oxidation of **5** with $NaIO_4$ gave compound **6** and further reacted with PEG^{2k}–NHS to obtain compound **7**. Treatment of rhodamine–NHS ester with compound **7** obtained compound **8**. Finally, compound **3** was added to compound **8** to obtain the final nanoprobe. The detailed description is shown in Scheme S1 in the (ESI†).

2.3 Characterization of NP1

2.3.1 Sodium dodecyl sulfate-polyacrylamide gel electrophoresis (SDS-PAGE). The purity of nanoprobes was determined by SDS-PAGE. **NP1** (25 μg) and IR-783 (1 μg), respectively in 25 μl treatment buffer (125 mM Tris, pH 6.8, 4% (w/v) sodium dodecyl sulfate (SDS), 20% (v/v) glycerol) were loaded on a 10% SDS-PAGE gel. After electrophoresis under a voltage of 70 V for 1 h, fluorescence images of the resulting SDS-PAGE gels were acquired by the Kodak *in vivo* multispectral imaging system equipped with an excitation filter (710–760 nm) and a 820 nm emission band pass filter set (FOV = 12.8 cm, f/stop = 4, bin = high resolution, exposure time = 2 s).

2.3.2 Dynamic light scattering (DLS). The hydrodynamic radius of **NP1** was determined by DLS. The measurements were performed at room temperature using a 20 s acquisition time. The standard solution of bovine serum albumin (BSA) in distilled water with a concentration 2.0 mg ml^{-1} was used for the calibration of the instrument. The samples were filtered through a 0.45 μm filter and diluted to 1.0 mg ml^{-1} by PBS pH 7.4. The hydrodynamic radius and the size distribution were calculated with the regularization algorithm provided by ZPW 388 software.

2.3.3 Absorbance spectroscopy. The UV-vis absorption spectra of **NP1** at different pH values were obtained on an ultraviolet-visible spectrometer (Shimadzu UV-2550 PC, Japan). The pH values were measured on a pH meter (Mettler Toledo MP120, Switzerland). A stock solution of **NP1** with a concentration of 2 mg ml^{-1} was prepared in 10 mM HEPES pH 8.3. The stock solution was diluted 100 times to PBS pH 7.4, 10 mM PBS pH 6.5, 10 mM MES pH 5.5, with a final concentration of 20 μg ml^{-1}.

2.4 PA system

The scheme of the photoacoustic microscopy (PAM) system is shown in Fig. S1 in the ESI.† An optical parametric oscillator (OPO) (VIBRANT B 532I, OPOTEK, USA) with a full-width at a high magnitude of 10 ns and a repetition of 10 Hz was used as the light source. The tuning range of the OPO ranged from 680 to

950 nm. Laser pulses from the laser were spatially filtered by a 25 μm diameter pinhole. Then, the light was focused by the objective lens to irradiate the tested sample. The energy of each laser pulse is detected by a photodiode for calibration. A focused ultrasound transducer with center frequency of 15 MHz and −6 dB bandwidth of 100% was used to receive the PA signals generated by the tested sample on the 3D scanning stage driven by computer-controlled stepper motors. The PA signals were recorded by the computer through the signal amplifier and a dual-channel data acquisition card. The sampling rate of the data acquisition card was 100 M samples s^{-1}.

2.5 pH dependent PA signal ratio and imaging studies

The solutions with a final concentration of 100 μg ml^{-1} were prepared at 10 mM PBS pH 7.4, pH 7.0, pH 6.5, 10 mM MES pH 6.0 and pH 5.5. As for the PA signal test, each solution was contained in a 0.5 mm diameter glass tube. The laser beam was focused to illuminate the solution and the focused ultrasonic transducer contacted the glass tube to receive the PA wave. At each acquisition point, the PA signals were averaged 128 times. The PA signal ratio was calculated by dividing the PA signal amplitudes under the dual-wavelength (785/708). As for dual-wavelength PA imaging, **NP1** solutions at pH 7.4, pH 6.5 and pH 5.5 with a concentration of 100 μg ml^{-1} were filled in a rounded container. All of the data were processed using the MATLAB program (version 7.0, Mathworks) with the maximum amplitude projection algorithm.

2.6 PA identifying cancer cells and normal cells

Murine mammary tumor line EMT-6 cells and Swiss mouse embryo line 3T3 cells were selected as cancer cells and normal cells, respectively. Cells cultured on 35 mm glass bottom culture dishes (14 mm microwell, MatTek, Ashland, MA) to approximately 70% confluence were treated with **NP1** (300 μg ml^{-1}) for 24 hours. At the end of treatment, the cells were washed with PBS 3× first and then the cells were embedded in a gel phantom for PA imaging at 708 nm and 785 nm.

2.7 *In vivo* PA identifying tumor

All animal experiments were carried out in accordance with guidelines evaluated and approved by the ethics committee of the South China Normal University. Murine mammary tumor line EMT-6 cells (5×10^6 cells in 50 μL PBS) were injected under the epidermis on the back of the mouse. The tumor was ready for PA experiments after inoculation for three weeks. Before PA experiments, the fur over the back of the mouse was shaven and chemically depilated. General anesthesia (i.p. sodium pentobarbital, 40 mg kg^{-1}; supplemental, 10 mg kg^{-1} h^{-1} or as necessary) was administered to keep the mouse motionless throughout the experiments. **NP1** (25 μg per mouse) was subcutaneously injected into the tumor region and normal tissue region. Both of them were imaged by PAM under the dual-wavelength.

2.8 Histological examination

After the mouse was sacrificed, tissue samples of tumor and normal tissue were obtained immediately. Specimens were fixed in Bouin's solution for 12 h. They were dehydrated, cleaned and then embedded in paraffin and finally sectioned to 4 mm thick perpendicular to the irradiation light axis. The sections were stained with hematoxylin and eosin (H and E), inspected and photographed under an optical microscope (ECLIPSE 80i, Nikon, Tokyo, Japan).

3. Results and discussion

The detailed synthesis procedure of **NP1** is depicted in the ESI.† Key features of dextran based **NP1** include the extra-close proximity of the two IR-783 labels in one D-glucopyranosyl unit and the multiple copies of such IR-783 modified units (Fig. 1). **NP1** as an exogenous contrast agent can be used for both NIR fluorescence imaging and PA imaging. Because of the intense light scattering in biological tissue, fluorescence imaging has a low imaging depth in tissue – up to ~1 mm, as defined by the optical diffusion limit. When incident photons reach this limit, most of them have undergone tens of scattering events, which scramble the photon paths and inhibit effective optical focusing, resulting in poor spatial resolution at depths beyond the optical diffusion limit.[37] PA imaging can break through the optical diffusion limit by capitalizing on the low acoustic scattering in tissue – about three orders of magnitude less than optical scattering in tissue per unit path length. The PA imaging depth is limited to the reach of photons and up to a few centimeters deep in biological tissues.[38] Furthermore, unlike fluorescence imaging, PA imaging ensures no leakage of excitation photons into detectors. By using **NP1** as contrast agents, dual-wavelength PA imaging shows the capacity of performing multicontrast and multidimensional *in vivo* scans of the tumor at depths from several millimeters to potentially centimeters with a resolution that can vary practically in the range 20–100 μm.[39] The acidic tumor microenvironment will promote the cleavage of hydrazone bonds and cause the IR-783 H-aggregates to change into monomers,[40,41] making the absorption coefficient of **NP1** change due to the acid–base property of the environment.

The purity of **NP1** is indicated by SDS-PAGE in Fig. 2a. The hydrodynamic diameters and size distributions of the **NP1** in aqueous dispersion were measured by a DLS technique shown in Fig. 2b. The DLS data suggest that the **NP1** was well dispersed in an aqueous dispersion with a narrow size distribution and a mean diameter of 9.936 nm. **NP1** demonstrated low cytotoxicity

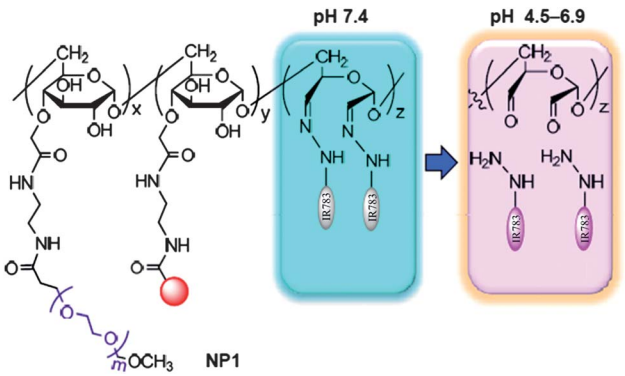

Fig. 1 The structure of **NP1**. The cleavage of hydrazone bonds in a physiologically acidic environment leads to the absorbance variation.

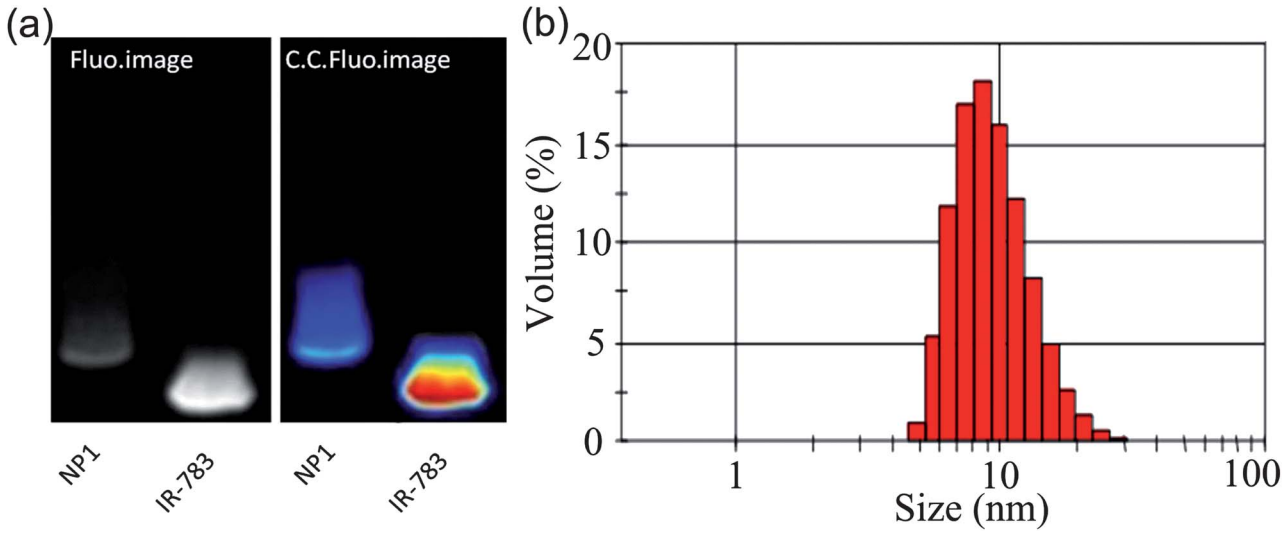

Fig. 2 (a) A representative fluorescent image of a SDS-PAGE gel loaded with the indicated nanoprobe (25 μg nanoprobe per well) and IR-783 (1 μg per well). The fluorescence and color coded (C. C.) fluorescence images of the resolved SDS-PAGE gel were collected by an optical imaging system with an exposure time of 2 s. (b) Hydrodynamic diameters and size distributions of **NP1** measured by dynamic light scattering in PBS pH 7.4. The average diameter of **NP1** is 9.936 nm.

and the cell viabilities stayed above 90% when the **NP1** concentrations were below 200 μg ml^{-1} (Fig. S2†).

The absorption spectra of **NP1** at physiologically relevant pHs of 7.4, 6.5 and 5.5 that mimic the normal physiological surroundings of tumor extracellular matrix and lysosomal compartments, are shown in Fig. 3a. UV-vis absorption spectra of **NP1** showed two resonance absorption peaks at 708 nm and 785 nm, which can be assigned to the H-aggregate and monomer of IR-783 and are different from that of IR-783 (776 nm) and rhodamine (542 nm), as shown in Fig. S3.† Compared with the absorption at 708 nm that decreased during the acidification procedure, the absorption at 785 nm increased remarkably, resulting in the significant increase of the absorption ratio between at 785 nm and 708 nm (A_{785}/A_{708}). The variation of the absorbance at the two wavelengths can be explained by the cleavage of hydrazone bonds followed by the de-association of aggregate and the releasing of the IR-783 monomer from **NP1** after further acidification. Fig. 3b shows the ratio of absorbance, which was normalized to its initial value at 0 min after incubation at 785 and 708 nm, increasing as a function of time after incubation, indicating the gradual cleavage course. The enhancement of the ratio at pH 5.5 is much higher than that in the other two pH values. Thus, **NP1** can generate tunable PA signals at two wavelengths due to the variation of the pH dependent absorbance.

Fig. 4a shows the recorded pH dependent PA signal amplitudes under 785 nm and 708 nm. With the same concentration, the PA amplitude of **NP1** excited by 785 nm increased in contrast with that excited by 708 nm. The statistical pH dependent PA signal intensity ratio (785 nm/708 nm) is shown in Fig. 4b. The ratio increased from 0.95 at pH 7.4 to 1.40 at pH 5.5. These results were explained by the fact that PA imaging has a high sensitivity to optical absorption and the absorption of **NP1** changed due to the pH value of the environment.

The pH dependent **NP1** for PA imaging is shown in Fig. 5. As shown in Fig. 5a, time resolved PA signals of **NP1** solution at

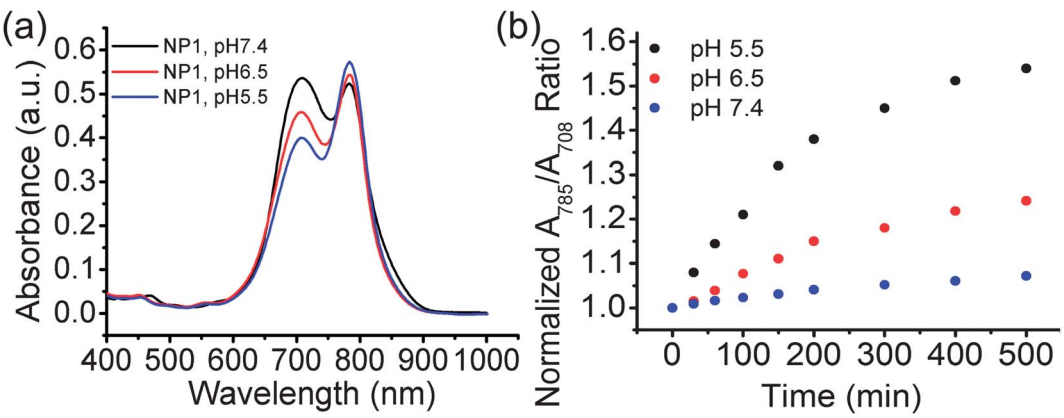

Fig. 3 (a) The absorbance of **NP1** (25 μg ml^{-1}) at pH 7.4, 6.5 and 5.5. (b) Ratio of absorbance at 785 and 708 nm (A_{785}/A_{708}) as a function of time in pH 7.4 (blue), 6.5 (red), 5.5 (black). The absorbance ratios were normalized to its initial value at 0 min after incubation.

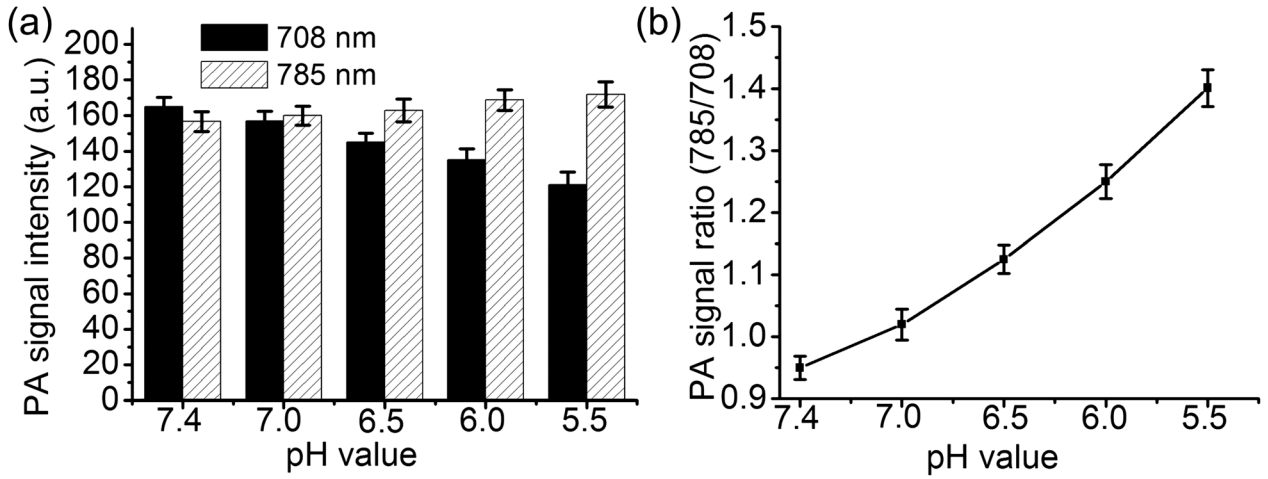

Fig. 4 (a) PA signal amplitude intensity at the two wavelengths of **NP1** at different pH values. (b) pH dependent PA signal ratios of **NP1** between 785 nm and 708 nm.

pH 5.5 excited at 708 nm and 785 nm can be clearly distinguished by comparing their amplitudes. Fig. 5b shows clear PA images both at 708 nm and 785 nm in aqueous solution. The PA signal generated at 785 nm clearly increased with the pH acidification. The tendency agreed well with the absorption spectrum shown in Fig. 3a. The above phenomenon contributed to the resonance absorption peaks of **NP1** at 708 nm and 785 nm and the varied absorption associated with further acidification. As previously reported, the NIR wavelength is one of the optimal regions for *in vivo* imaging.[22,42] A pH-sensitive PA probe may further minimize the background signal resulting from the intrinsic optical absorption in tissues and has the potential to be a useful tool for *in vivo* biomedical imaging with **NPl** as a contrast agent.

Previous work showed the lysosomal delivery of the dextran based nanoprobe (Fig. S4†). Since highly aggressive cancer cells usually exhibit a more acidic lysosomal lumen (pH 4.5–5.5) than normal cells (pH 5.0–6.0),[43] the absorption ratio of **NP1** in cells between 708 nm and 785 nm may be changed due to the environmental pH variation. The feasibility of **NP1** for PA imaging to detect and distinguish normal cells and cancer cells *in vitro* is demonstrated in Fig. 6a. This nanoprobe visualized both normal cells and cancer cells under the dual-wavelength, but the contrast (785 nm/708 nm) in cancer cells is significantly higher than that in normal cells, which is attributed to the tunable absorption of **NP1** at the two wavelengths. To quantitatively compare the differences, the statistical PA signal amplitude ratio in the interesting region between 785 nm and 708 nm was analyzed, as shown in Fig. 6b. Compared to normal cells, cancer cells possessed a higher ratio, which is in agreement with the pH value of lysosomes in normal cells and cancer cells. These results indicate that dual-wavelength PA imaging is capable of differentiating the normal cells and cancer cells using **NP1** as PA probes.

The potential application of **NP1** as a pH-sensitive PA probe for tumor identification *in vivo* was investigated. Fig. 7a shows a photograph of a Murine mammary tumor-bearing mouse. Compared with the tumor region indicated by the blue circle, the normal muscle tissue indicated by the black circle was selected as a control. After subcutaneous administration of **NP1**, normalized time dependent PA signal ratios of tumor and normal muscle tissue were analyzed, as shown in Fig. 7b. The ratio in the tumor increased and reached 1.124 at 500 min post-injection, while in normal muscle tissue the ratio just increased to 1.05. These results indicated the cleavage of IR-783 H-aggregates and the releasing of the IR-783 monomer from **NP1** in the acidic surrounding of the tumor. After 500 min post-injection, PA

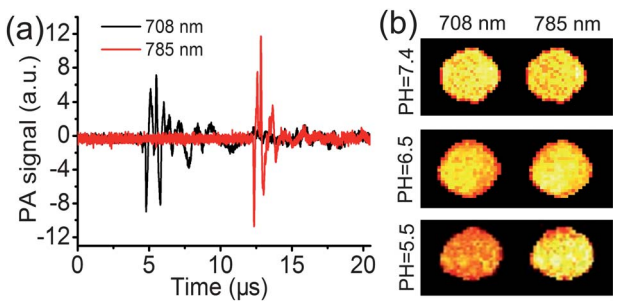

Fig. 5 (a) Time resolved PA signals of **NP1** solution at pH 5.5 excited at 708 nm and 785 nm. (b) PA images of **NP1** at pH 7.4, 6.5 and 5.5. All of the solutions were incubated for 24 h and with a concentration of 100 μg ml^{-1}.

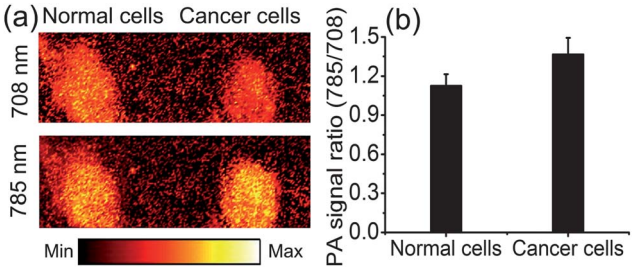

Fig. 6 (a) Dual-wavelength PA images of normal cells (Swiss mouse embryo line 3T3) and cancer cells (Murine mammary tumor line EMT-6) incubated with **NP1** (300 μg ml^{-1}) for 24 h. (b) Quantification studies showing the significantly higher PA signal ratio of cancer cells than that of normal cells under dual-wavelength. Data are expressed as the mean ± SD and the bars show the SD.

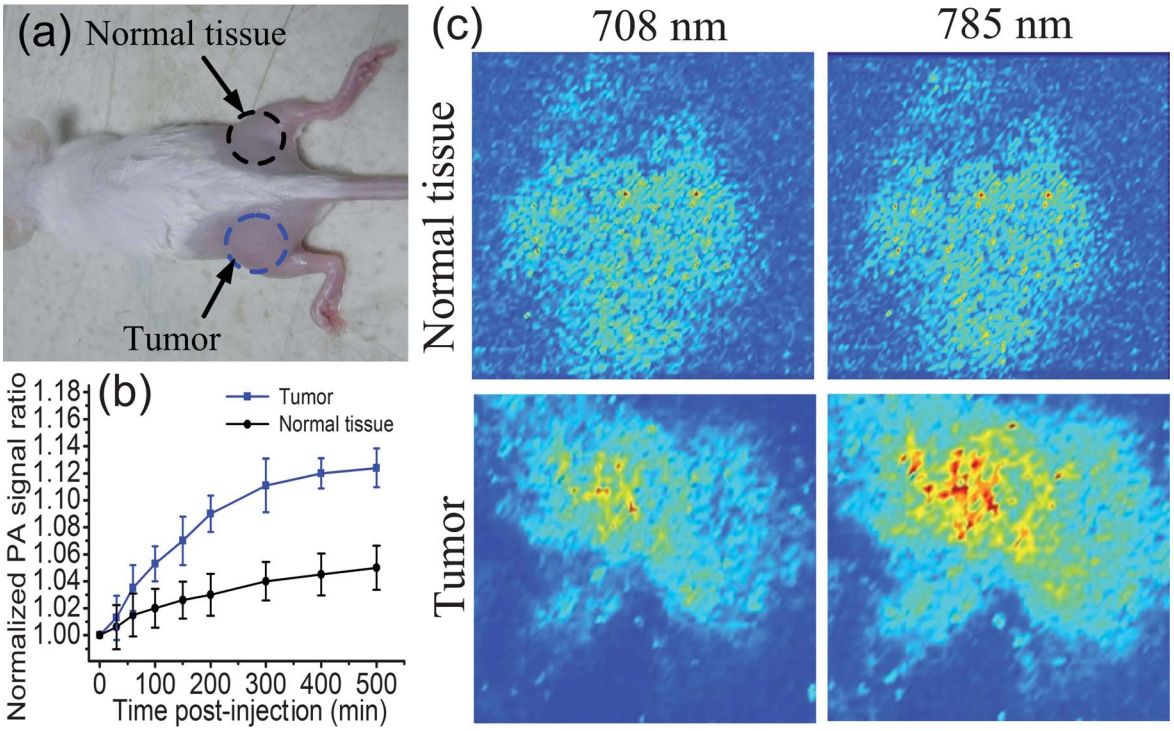

Fig. 7 (a) A photograph of a tumor-bearing mouse. (b) Time dependent PA signal ratio between tumor and normal tissue under dual-wavelength. (c) PA images of the tumor and normal tissue after **NP1** administration.

images were taken both in the tumor and in the normal tissue region at the two wavelengths. Both the tumor and normal tissue were clearly depicted by PA imaging shown in Fig. 7c, which employs the resonance absorption of **NP1** at the designated wavelength. As the different pH values between tumor and normal tissue can make **NP1** with a different absorption ratio, the difference in PA images of the tumor at the dual-wavelength is much more obvious than that in normal tissue. H and E stained histological sections of tumor and normal tissue verified the different tissue characterization in Fig. S5 in the ESI.† The above *in vivo* studies clearly indicate the feasibility of using **NP1** as a PA nanoprobe to identify tumors through pH-sensitive dual-wavelength PA imaging.

4. Conclusions

In conclusion, we have demonstrated a pH-sensitive nanoprobe as a PA imaging agent. **NP1** with pH-sensitive dual NIR resonance absorption exhibits strong pH dependent PA signals. By sensing the physiologically acidic environment, **NP1** shows tunable optical absorbance under the dual-wavelength and is capable of distinguishing between normal cells and cancer cells and identifying a solid tumor *in vivo* by dual-wavelength PA imaging. Thus, pH-sensitive **NP1** holds promise for the early detection and diagnosis of cancer.

Acknowledgements

This research is supported by the National Basic Research Program of China (2011CB910402; 2010CB732602), the Program for Changjiang Scholars and Innovative Research Team in University (IRT0829) and the National Natural Science Foundation of China (81127004; 11104087).

Notes and references

1 M. R. Oliva and S. Saini, *Cancer Imaging*, 2004, **4**, s42–s46.
2 F. Ye, S. Yang and D. Xing, *Appl. Phys. Lett.*, 2010, **97**, 213702.
3 H. P. Schlemmer, *Cancer Imaging*, 2011, **11**, s153.
4 L. Yao, Y. Sun and H. Jiang, *Opt. Lett.*, 2009, **34**, 1765–1767.
5 E. I. Galanzha, E. V. Shashkov, T. Kelly, J. Kim, L. Yang and V. P. Zharov, *Nat. Biotechnol.*, 2009, **4**, 855–860.
6 L. Li, K. Maslov, G. Ku and L. V. Wang, *Opt. Express*, 2009, **17**, 16450–16455.
7 K. Kim, S. W. Huang, S. Ashkenazi, M. O'Donnell, A. Agarwal, N. A. Kotov, M. F. Denny and M. J. Kaplan, *Appl. Phys. Lett.*, 2007, **90**, 223901.
8 Y. Zhang, X. Cai, Y. Wang, C. Zhang, L. Li, S.-W. Choi, L. V. Wang and Y. Xia, *Angew. Chem., Int. Ed.*, 2011, **50**, 7359–7363.
9 Y. Yuan, S. Yang and D. Xing, *Appl. Phys. Lett.*, 2012, **100**, 023702.
10 S. Yang, F. Yei and D. Xing, *Opt. Express*, 2012, **20**, 10370–10375.
11 A. Zerda, Z. A. Liu, S. Bodapati, R. Teed, S. Vaithilingam, B. T. Khuri-Yakub, X. Y. Chen, H. J. Dai and S. S. Gambhir, *Nano Lett.*, 2010, **10**, 2168–2172.
12 A. Taruttis, S. Morscher, N. Burton, D. Razansky and V. Ntziachristos, *PLoS One*, 2012, **7**, e30491.
13 L. Nie, Z. Guo and L. V. Wang, *J. Biomed. Opt.*, 2011, **16**, 076005.
14 T. Islam and M. G. Harisinghani, *Cancer Biomarkers*, 2009, **5**, 61–67.
15 P. Sharma, S. C. Brown, N. Bengtsson, Q. Zhang, G. A. Walter, S. R. Grobmyer, S. Santra, H. Jiang, E. W. Scott and B. M. Moudgil, *Chem. Mater.*, 2008, **20**, 6087–6094.
16 L. Nie, Z. Ou, S. Yang and D. Xing, *Med. Phys.*, 2010, **37**, 4193–4200.
17 T. Zhou, B. Wu and D. Xing, *J. Mater. Chem.*, 2012, **22**, 470–477.
18 Z. Wang, C. Liu, L. Chang and Z. Li, *J. Mater. Chem.*, 2012, **22**, 12186–12192.
19 X. Yu, L. Chen, M. Li, M. Xie, L. Zhou, Y. Li and Q. Wang, *Adv. Mater.*, 2008, **20**, 4118–4123.

20 N. Saito, Y. Usui, K. Aoki, N. Narita, M. Shimizu, K. Hara, N. Ogiwara, K. Nakamura, N. Ishigaki, H. Kato, S. Taruta and M. Endo, *Chem. Soc. Rev.*, 2009, **38**, 1897–1903.
21 Z. Liu, S. Tabakman, S. Sherlock, X. Li, Z. Chen, K. Jiang, S. Fan and H. Dai, *Nano Res.*, 2010, **3**, 222–233.
22 C. Kim, H. Song, X. Cai, J. Yao, A. Wei and L. V. Wang, *J. Mater. Chem.*, 2011, **21**, 2841–2844.
23 G. Huang, S. Yang, Y. Yuan and D. Xing, *Appl. Phys. Lett.*, 2011, **99**, 123701.
24 L. Xiang, Y. Yuan, D. Xing, Z. Ou, S. Yang and F. Zhou, *J. Biomed. Opt.*, 2009, **14**, 021008.
25 C. Kim, E. C. Cho, J. Chen, K. H. Song, L. Au, C. Favazza, Q. Zhang, C. M. Cobley, F. Gao, Y. Xia and L. V. Wang, *ACS Nano*, 2010, **4**, 4559–4564.
26 H. Maeda, J. Wu, T. Sawa, Y. Matsumura and K. Hori, *J. Controlled Release*, 2000, **65**, 271–284.
27 Q. Zhang, N. Iwakuma, P. Sharma, B. M. Moudgil, C. Wu, J. M. Neill, H. Jiang and S. R. Grobmyer, *Nanotechnology*, 2009, **20**, 395102.
28 E. C. Cho, C. Kim, F. Zhou, C. M. Cobley, K. H. Song, J. Chen, Z. Li, L. V. Wang and Y. Xia, *J. Phys. Chem. C*, 2009, **113**, 9023–9028.
29 S. Link and M. A. El-Sayed, *Int. Rev. Phys. Chem.*, 2000, **19**, 409–453.
30 C. Buzea, I. I. Pacheco and K. Robbie, *Biointerphases*, 2007, **2**, MR17–MR71.
31 R. A. Gatenby and R. J. Gillies, *Nat. Rev. Cancer*, 2004, **4**, 891–899.
32 N. C. Denko, *Nat. Rev. Cancer*, 2008, **8**, 705–713.
33 C. Li, J. Xia, X. Wei, H. Yan, Z. Si and S. Ju, *Adv. Funct. Mater.*, 2010, **20**, 2222–2230.
34 M. A. Casadei, G. Pitarresi, R. Calabrese, P. Paolicelli and G. Giammona, *Biomacromolecules*, 2008, **9**, 43–49.
35 S. Mitra, U. Gaur, P. C. Ghosh and A. N. Maitra, *J. Controlled Release*, 2001, **74**, 317–323.
36 S. Achilefu, *Technol. Cancer Res. Treat.*, 2004, **3**, 393–409.
37 N. J. Durr, C. T. Weisspfennig, B. A. Holfeld and A. Ben-Yakar, *J. Biomed. Opt.*, 2011, **16**, 026008.
38 L. V. Wang and S. Hu, *Science*, 2012, **335**, 1458–1462.
39 D. Razansky, M. Distel, C. Vinegoni, R. Ma, N. Perrimon, R. W. Koster and V. Ntziachristos, *Nat. Photonics*, 2009, **3**, 412–417.
40 Z. Zhang and S. Achilefu, *Chem. Commun.*, 2005, (47), 5887–5889.
41 A. Almutairi, S. J. Guillaudeu, M. Y. Berezin, S. Achilefu and J. Frchet, *J. Am. Chem. Soc.*, 2008, **130**, 444–445.
42 K. Chung, M. Cho, M. Sung, H. Poo and Y. Lim, *Chem. Commun.*, 2011, **47**, 8889–8891.
43 K. Glunde, S. E. Guggino, M. Solaiyappan, A. P. Pathak, Y. Z. Ichikawa and M. Bhujwalla, *Neoplasia*, 2003, **5**, 533–545.